

## Pulse-Front Propagation and Interaction During the Growth of CdS Nanoparticles in a Gel

Mazen Al-Ghoul,<sup>\*†‡</sup> Tarek Ghaddar,<sup>†</sup> and Tharwat Moukalled<sup>†</sup>

Department of Chemistry, and Center for Advanced Mathematical Sciences, American University of Beirut, Beirut, Lebanon

Received: March 13, 2009; Revised Manuscript Received: July 9, 2009

We studied the spatiotemporal dynamics of a new system consisting of sulfide ions (outer electrolyte) diffusing into an organic gel (gelatin) containing mercaptoethanol-capped cadmium ions (inner electrolyte). The product, cadmium sulfide, exhibits a faint yellow transparent propagating front starting at the gel–outer electrolyte interface. When subjected to UV light, this system reveals fluorescing CdS nuclei localized spatially in a narrow region, called pulse, that leads the front and propagates down the tube. We show that the pulse consists of CdS nanoclusters of an average size of about 4 nm, whereas the trailing front consists of 6–8 nm cubic-phase CdS crystallites. The width of the pulse remains constant in time,  $t$ , at about 2 mm and independent of the outer concentration  $S_0$ . It was found that the speed of the pulse fluctuates as the concentration of the capping agent is varied, with fastest pulses attained at a concentration of 40 mM for two different outer concentrations of sulfide ions. The origin of the yellow fluorescence of the pulse originates from emission from surface states. This dynamical system was then theoretically studied using a competitive particle growth model. The resulting evolution equations were solved numerically, and the results were compared to the experimental findings. It was shown that the model agrees in many aspects with the experiment. The densities of small particles  $\tilde{\rho}$  and large particles  $\rho$  were shown to evolve like a pulse and a front, respectively. The front was shown to extend “diffusively” as  $t^{1/2}$ , as found experimentally. The distance traveled by the pulse  $x_{\text{peak}}$  was shown to increase with outer concentration  $S_0$  and obeys a concentration power law  $x_{\text{peak}} \sim S_0^{1/4}$ . The width  $w$  of the pulse also obeys a time power law  $w \sim t^a$  with a crossover between early times ( $a = 1/3$ ) and intermediate times ( $a = 0$ ). This system would enable us to study the early time dynamics of Liesegang systems.

### 1. Introduction

In the last two decades, moving diffusion reaction fronts (or pulses) of the type  $A + B \rightarrow C$  with initially separated reactants have attracted a great deal of interest and concomitant experimental<sup>1–7</sup> and theoretical<sup>8–11,13,14</sup> research. It was conceived that pattern formation in the trail of the front, which can exhibit a multitude of complex and rich dynamics, is a general phenomenon in chemistry,<sup>15,16</sup> biology,<sup>17,18</sup> geology,<sup>19–21</sup> materials science,<sup>22,23</sup> and engineering.<sup>24–26</sup>

In chemistry, there are systems where the product C is a 1:1 complex in the solution phase. Examples include the  $\text{Cu}^{2+}$ –tetra,<sup>1,4,6</sup>  $\text{Cr}^{3+}$ –xylenol orange (XO),<sup>2</sup> and  $\text{Ca}^{2+}$ –Ca green<sup>5,7</sup> systems. In those reactions, the colored complex makes the front distinctly visible, and the kinetics is thus monitored spectrophotometrically. There are also other types which involve precipitation of the product. In particular, the Liesegang banding patterns<sup>27</sup> are thought to be a result of an interplay between the front’s dynamics, nucleation, and growth of the precipitate. Accordingly, this type of system belongs to a group of reactions where the product C is a solid, and hence, the moving front is located at the solid–solution interface. Such experiments usually take place in a gel medium containing a dissolved ionic species that is invaded by another diffusing coprecipitate ionic species; a uniform precipitation front and sometimes Liesegang bands are formed.<sup>27–29</sup> Crossover between a spatially uniform pulse and a pattern of periodic bands is observed as the concentration

gradient increases through zero in the study by López Cabarcos et al.,<sup>3</sup> where they examined the propagation of a  $\text{CaHPO}_4$  deposit in an agarose gel channel from initially separated  $\text{Ca}^{2+}$  and  $\text{HPO}_4^{2-}$ . In this work, several scaling laws for the time of formation of the precipitate as well as its width were determined. For a zero gradient, the deposit zone became narrower as the concentration of the reactants increased.

The experimental studies focus on the width, height, and location of the front, as well as the global reaction rate, along with their time dependence.<sup>4</sup> A crossover between an early irreversible regime and a late reversible regime was demonstrated<sup>1</sup> and conjectured.<sup>13</sup> The critical scaling exponents were also found to exhibit such a crossover.<sup>12</sup> Nontrivial crossovers between irreversible regimes along with different classes of universality were reported and conjectured by Taitelbaum and his co-workers.<sup>31,32</sup>

In this paper, we present a study of the spatiotemporal dynamics of front propagation of CdS nanoparticles (or quantum dots) in gelatin (an organic gel). The interest in this system stems from the fact that cadmium sulfide quantum dots are semiconductor nanoparticles with diameters less than about 10 nm with unique size-dependent optoelectronic properties<sup>33</sup> that allowed us to follow experimentally its growth starting from nuclei to larger crystallites. In addition, as size changes, the surface to bulk atom ratio also changes, which is pronounced in changes in thermal and mechanical properties. The technological potentials of semiconductor quantum dots are in photocatalysis, solar energy conversion, nonlinear optical devices, and so forth.<sup>34</sup> Various methods<sup>35</sup> were used to tailor the size of semiconductors by controlling their precipitation. These include the control of

<sup>\*</sup> To whom correspondence should be addressed.

<sup>†</sup> Department of Chemistry.

<sup>‡</sup> Center for Advanced Mathematical Sciences.

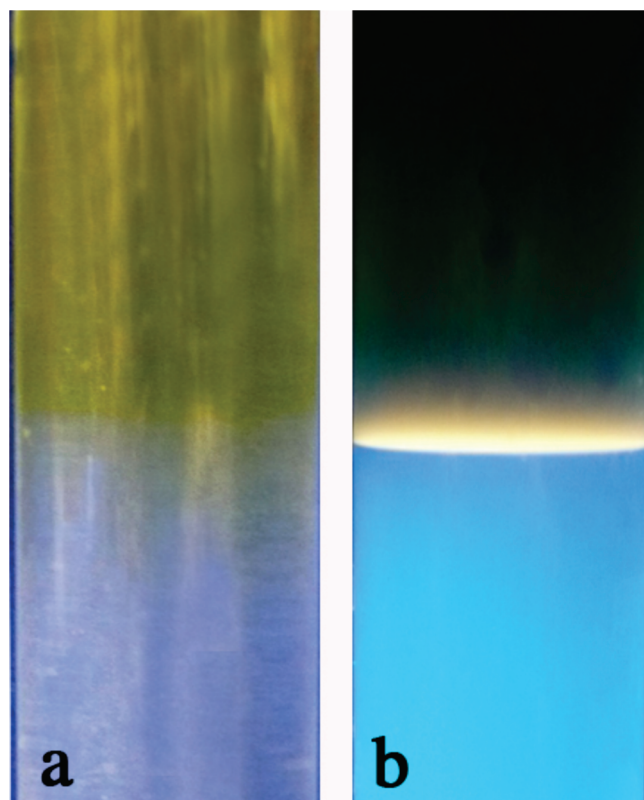


**Figure 1.** A typical front-pulse propagation during the reaction–diffusion of sulfide and capped cadmium ions. The initial concentrations are  $[S^{2-}] = 50 \text{ mM}$ ,  $[Cd^{2+}] = 2.0 \text{ mM}$ , and  $[\text{Mercaptoethanol}] = 40.0 \text{ mM}$ . (a) The transparent yellow front invading the tube downward. (b) The same tube when illuminated with UV light. The fluorescing pulse leads the front. The photoluminescence of the gel is seen below the pulse. Quenching in the region above the pulse is also clear.

the particle growth using stabilizers or matrixes, such as thiols, phosphine oxides, zeolites, glasses, polymers, reverse micelles, vesicles, films, multilayer films, aerogels, and silica; size fractionation by using exclusion chromatography or gel electrophoresis; and size-selective precipitation or photocorrosion.

Our system consists of a long thin tube containing Cd(II) ions embedded in gelatin with mercaptoethanol acting as a capping agent,<sup>36</sup> above which a solution of sulfide ions is added. As a result, a clear yellow front slowly invades the tube downward. When the tube is subjected to UV light, we discover that this front is led by a fluorescing pulse of fixed width. A continuous growth of CdS nanoparticles in the wake of the propagating front is thus expected to take place.

This paper is divided into two parts, the experimental study of the dynamics of pulse propagation of CdS nanoclusters and their growth into a front of larger crystallites. The second part consists of the theoretical modeling of the propagating front in which the nucleation and growth are incorporated. The theoretical results are then compared to the experimental findings. Therefore, the system we report in this paper consists of a pulse/front propagation followed by nucleation and growth of CdS nanoparticles, which constitutes a higher level of complexity than the aforementioned experimental and theoretical systems.

## 2. Experimental Section

**2.1. Instrumentation.** Emission spectra were measured on a Jobin–Yvon Horiba Fluorolog-3 spectrophotofluorometer. UV/vis spectra were recorded on a Jasco V-570 UV/vis/NIR. Time-correlated single-photon counting (TCSPC) emission decay

**TABLE 1: Different Compositions in Initial Reactants in 14 Tubes**

tube #	$[\text{CdCl}_2]/(\text{mM})$	$[\text{Na}_2\text{S}/(\text{mM})$	$[\text{mercaptoethanol}]/(\text{mM})$
1	2.0	50	2.5
2	2.0	50	5.0
3	2.0	50	10.0
4	2.0	50	20.0
5	2.0	50	40.0
6	2.0	50	80.0
7	2.0	50	160.0
8	2.0	20	2.5
9	2.0	20	5.0
10	2.0	20	10.0
11	2.0	20	20.0
12	2.0	20	40.0
13	2.0	20	80.0
14	2.0	20	160.0

measurements were done using an IBH NanoLED-405 diode laser for the excitation source and an IBH TBX-04 photomultiplier detector, where the emission detection wavelength was set to 560 nm. The XRD data were recorded by a Bruker d8 discover X-ray diffractometer equipped with a Cu K $\alpha$  radiation ( $\lambda = 1.5405 \text{ \AA}$ ).

**2.2. Tube Preparation.** A 5% gelatin (Difco) solution was prepared in doubly distilled water (resistivity,  $18 \text{ M}\Omega \text{ cm}$ ), where the gelatin was accurately weighed, added to water, and then heated with constant stirring until the solid dissolved completely. Preweighed anhydrous  $\text{CdCl}_2$  (Merck) was added to the gelatin suspension followed by mercaptoethanol (Acros). After the solution homogenized (5 min), the solution was poured, while hot, into a thin tube (length = 20.0 cm and inner diameter = 50 mm) and then allowed to cool and stand for at least 12 h in a thermostat set at 20 °C. Finally, sodium sulfide ( $\text{Na}_2\text{S} \cdot 9\text{H}_2\text{O}$ ) (Alfa Aesar) in doubly distilled water containing mercaptoethanol was added on top of the solidified gel and stored in the thermostat. The concentration of mercaptoethanol inside of the gel and above was always kept the same to prevent diffusion of the capping agent.

## 3. Results and Discussion

The investigation of the test tubes in the presence and absence of UV light had started as soon as the sulfide solution was added above the gel solution. Early on, a transparent yellow front invades the tube downward, as shown in Figure 1a. The content of this front is suspected to be CdS with a small particle size and shall be later analyzed. When the tube is subject to UV light ( $\lambda = 360 \text{ nm}$ ), a thin fluorescing yellow pulse is observed ahead of the aforementioned CdS front. The term “front” is used to indicate a connection or transition connecting the bulk region and the nuclei region. Moreover, gelatin ahead of the pulse (i.e., not yet invaded by the reaction front) exhibits photoluminescence of blue light, as shown in Figure 1b. The term “pulse” is used here to indicate a spatially localized region that propagates forward akin to a solitary wave. On the other hand, very weak fluorescence originating from either the particles in the front or the gel was observed in the front region preceding the pulse, indicating that there could be luminescence quenching due to particles formed in the front larger than those in the pulse. The pulse seems to lead the front until the end of the tube is reached. On that account, it appears that the coupling between diffusion and reaction of sulfide and capped cadmium ions leads, in the described setup, to a crystal growth mechanism whereby larger crystals of CdS are formed from smaller clusters born in a thin moving reaction region (the pulse). The reaction process taking

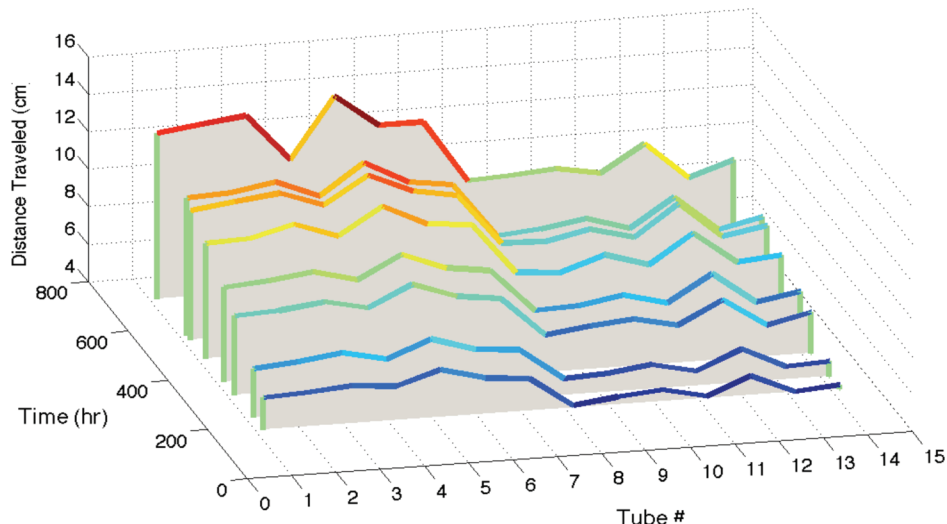


**Figure 2.** Plot of the distance (cm) traveled by the pulse versus time (h) and tube number. The composition of the tubes is given in Table 1.

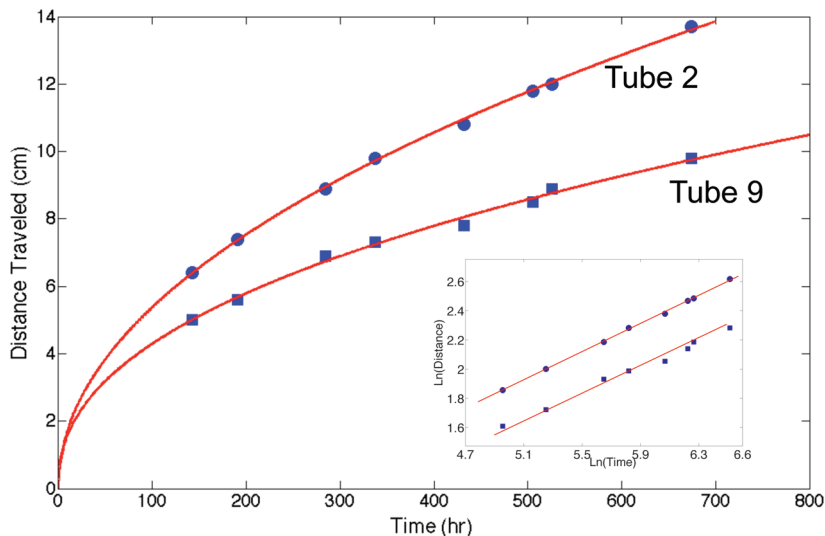


**Figure 3.** Distance traveled versus time for tube 2 (circle) and tube 9 (square) differing only in the outer concentrations. The inset shows the linear fit to the  $\ln-\ln$  plot for tubes 2 and 9. The slopes of the fitted lines are 0.48 and 0.42, respectively.

place can thus be split into two parts; the first part describes the reaction of the diffusing ions to form nuclei of the product. This is represented by the fluorescing pulse. In the second part, a growth of nuclei into larger particles takes place, and this is represented by the front. In what follows, we shall explore and verify such a mechanism by analyzing the speed of propagation of the pulse and front and their widths and content and then present a theoretical model of the process.

**3.1. Speed of the Pulse.** A broad region of varying concentration was first explored where different outer concentrations of  $\text{Na}_2\text{S}$  (ranging from 8 to 200 mM) and of mercaptoethanol (ranging from 2.5 to 200 mM) were used while the inner concentration of  $\text{CdCl}_2$  was fixed to 2 mM. No major effects on the propagating front were seen in these concentration ranges. However, increasing the mercaptoethanol concentration beyond 0.2 M destroyed the gelatin constituency. Consequently, we decided to focus our investigation throughout this work on the following sets of concentrations summarized in Table 1.

We measured the distance traveled by the pulse in the case of the 14 tubes in Table 1, which, in fact, can be split into two subgroups (GI: tubes 1–7; GII: tubes 8–14) differing in the outer concentration of the sulfide ions. The results are summarized in Figure 2. It is clear that the speed of the pulse

increases when the outer concentration of the sulfide ions increases (GI as compared to GII). This is expected due to the larger diffusion flux resulting from a higher concentration gradient. It is also noticeable in this figure that the oscillations in the distance traveled as a function of the concentration of mercaptoethanol; however, for both subgroups GI and GII, the highest velocity was obtained for tubes 5 and 12, where  $[\text{mercaptoethanol}] = 40.0 \text{ mM}$ , emphasizing the complicated role of the capping agent in the dynamics of this reaction–diffusion system. These oscillations were experimentally reproducible. We repeated the experiment 10 times over several months. In all of these experiments, oscillations were exhibited, and in most of the experiments, the results did not show any quantitative difference. Apparently, the capping agent is interfering in the dynamics of the system in a complicated manner, and these are, in fact, very peculiar and interesting. However, in order to understand these fluctuations, different capping agents should be used and compared.

On the other hand, for any given tube, the distance traveled versus time exhibit a diffusion-like profile, that is,  $d \sim t^\beta$ , where  $\beta \approx 1/2$ , as shown in Figure 3 in the case of tubes 2 and 9 where the difference is in the outer concentration but with same concentration of the capping agent. It is clear in this figure that

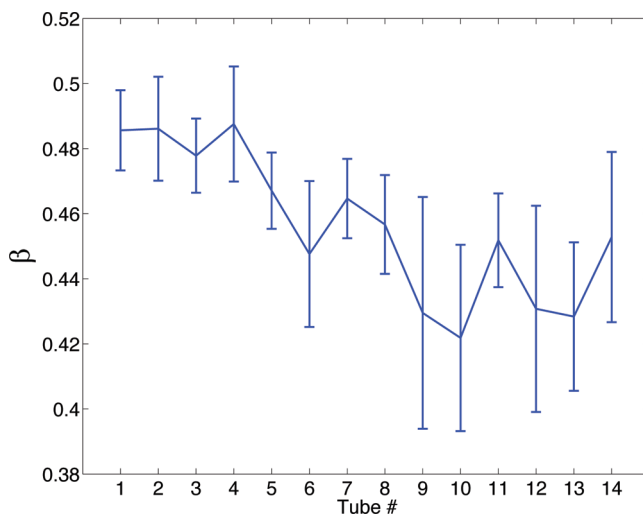


**Figure 4.** Exponent  $\beta$  of the log–log fit of the distance traveled versus time for the 14 tubes of Figure 2. The power close to 0.5 is indicative of diffusion. The error bars are plotted using the 95% confidence intervals for the coefficient estimates of the best fit.

for a ratio of the outer concentration of 2.5 (tubes 2 and 9), the distance traveled by the front increases on average by 30% after a lapse of 500 h as the front reaches the end of the tube. Figure 4 shows the exponents of the best fit to the diffusion profiles (distance traveled versus time), which is extracted as the slope of the log–log plot of the profile for the 14 tubes. For all the 14 tubes, the exponent was found to be less than or equal to 1/2. The reason why the exponent  $\beta$  determined in Figure 4 never exceeds the 1/2 could be attributed to two factors. First, it could be due to a deviation from a strict bimolecular mechanism between the  $\text{Cd}^{2+}$  and  $\text{S}^{2-}$  ions due to the interaction with the capping agent and/or the gel; second, it could be lowered due to the porosity of the gel, which imposes an anomalous diffusion exponent of  $d_w < 2$ , which, in turn, produces an anomalous diffusion exponent of  $1/d_w$  rather than 1/2 as argued by Hecht et al.<sup>37</sup>

**3.2. Width of the Pulse.** The pulse was always concentrated in a very narrow region on the order of a millimeter and accompanied by a fluorescing haze (similar to a comet). The width of this pulse was measured systematically according to a visual criterion whereby the aforementioned haze behind the pulse was ignored. The width was found to be constant throughout the propagation. It was found to be equal to 2 mm. It was also found to be independent of the outer and inner concentrations as well as the viscosity of the gel matrix. Using the scaling relations of Gálfy and Rácz<sup>8</sup> for the simple reaction  $\text{A} + \text{B} \rightarrow \text{C}$ , which was later generalized by Bazant and Stone in their seminal paper<sup>38</sup> on the reaction of the form  $m\text{A} + n\text{B} \rightarrow \text{C}$ , where the diffusion coefficients of reacting species were  $D_{\text{A}} > 0$  and  $D_{\text{B}} = 0$ , the width of the reaction pulse (called front in the original paper), which is defined as the spatially localized region where the production of C is nonzero, was  $w \sim t^{\alpha}$ , where  $\alpha = (m - 1)/2(m + 1)$ , and the center of the front diffused as  $x_f \sim t^{1/2}$  for sufficiently long times and for any given ratio of initial concentrations. These results were also confirmed numerically by Jiang and Ebner<sup>39</sup> using random walks on a two-dimensional lattice. If  $m = 1$ , as anticipated in  $\text{Cd}^{2+}/\text{S}^{2-}$  reaction,  $\alpha = 0$ , meaning that the reaction front's width does not change for a sufficiently long time. We can infer from this result that the  $\text{Cd}^{2+}$  ions are somewhat localized in the gelatin matrix possibly due to the interaction between these ions and specific functional groups on gelatin. When these ions react

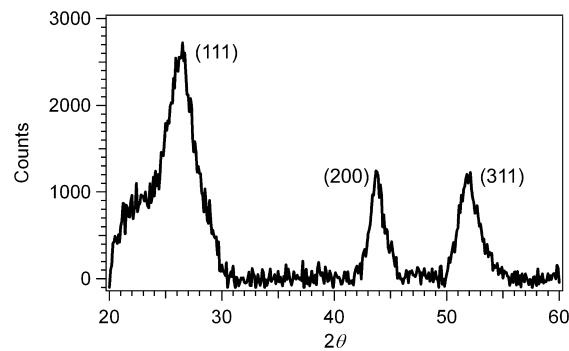


**Figure 5.** X-ray diffraction spectrum of CdS in the front region above the pulse. The peaks at 26.5, 44, and 52° reveal that CdS is in the cubic phase.

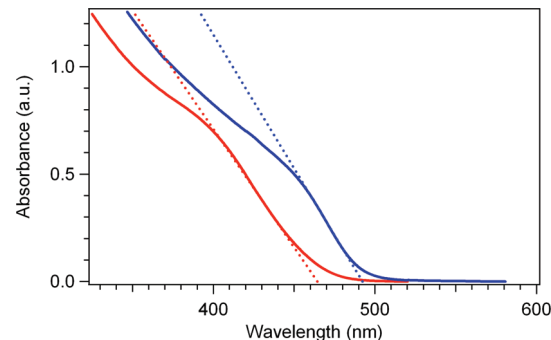


**Figure 6.** Absorption spectra of the propagating pulse (red) and the front region above the pulse (blue) for tube 1. The cutoff wavelengths for the pulse and front are  $\lambda = 464.5$  and  $492.5$  nm, respectively. The dotted lines are used for extrapolating the cutoff wavelengths.

with the invading  $\text{S}^{2-}$  ions, nucleation of colloidal CdS particles takes place in the narrow pulse, and they become partially mobilized in the matrix. This proposed mechanism is endorsed by the fluorescence spectra discussed in the next section. These nucleating clusters lead the way to larger CdS particles in its wake.

**3.3. Particle Growth. 3.3.1. X-ray Diffraction Measurements.** The X-ray diffraction (XRD) spectrum of the suspended particles in the region above the pulse is shown in Figure 5. Three broad peaks at  $2\theta = 27, 44$ , and  $52^\circ$  belonging to (1 1 1), (2 2 0), and (3 1 1) Miller indices of a cubic zinc-blende-type structure (JCPDS file no. 10454) are seen. The broad feature of the bands is indicative of the small size of the particles since it is known that the XRD peaks' intensity decreases and the width increases with decreasing crystalline size. The broadening of XRD peaks can be qualitatively expressed by Debye–Scherrer's formula  $D = K\lambda/\beta\cos \theta$ , where  $D$  is the average crystal size,  $\lambda$  is the wavelength of X-rays used,  $\beta$  is the full width at half-maxima (fwhm) of the XRD peak,  $\theta$  is the Bragg angle, and  $K$  is the shape factor, which has the value close to 1. The average crystal size in the region above the pulse was computed from the broadening of the peak at  $2\theta = 44^\circ$  corresponding to the (220) plane and was found to be about 6 nm, consistent with the estimate with the UV–vis spectra below. Although a CdS crystal size above 5 nm favors the hexagonal phase,<sup>40</sup> the cubic phase of the crystals trapped in the gel above the pulse does not change for many weeks. The temperature at which this experiment is performed is low ( $20^\circ\text{C}$ ), and thereby, the rate of nucleation/growth and the rate of phase transformation are both relatively small. If a phase transformation from the cubic to the hexagonal phase is to take place, the nucleation of the latter phase is initiated at the nanocrystal surface. The protection provided by the gel matrix against phase changes

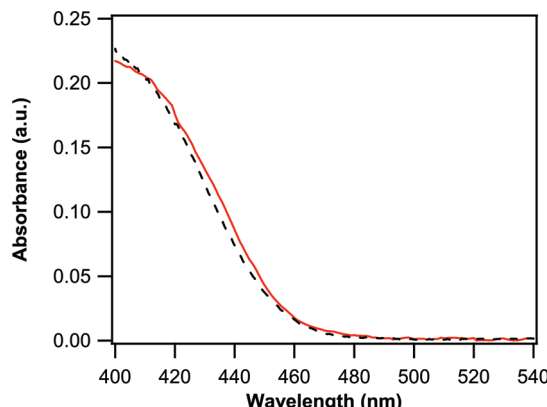


**Figure 7.** Absorption spectra of the propagating front in tube 1 on day 7 (solid red) and on day 22 (dashed black).

from the cubic to the hexagonal phase is attributed mainly to three reasons. First, the gel forms a barrier between the clusters of the CdS nanoparticles, forbidding them from coalescing, especially at low concentration of the CdS, that is, below the percolation threshold. The second reason lies in the high viscosity of the gel, which decreases the mobility of the atoms on the surface of the nanocrystals. This fact is particularly enforced because of the expected strong interaction between gelatin and the CdS clusters. Porosity of the gel is also expected to play a role in the aforementioned protection because the smaller the pores (with low density) are, the smaller the surface mobility is for the nanocrystals entrapped within, thus inhibiting phase transformation. We could not take an XRD spectrum of the particles in the front due to their small size and dilute concentration.

**3.3.2. UV/Vis Absorption.** Figure 6 shows the UV/vis absorption spectra of the propagating pulse (red curve) and the region above the pulse (blue curve) in the gelatin matrix. The cutoff wavelength for the pulse was measured to be  $\lambda = 464.5$  nm, which corresponds to nanocrystals of sizes  $d \leq 4.7$  nm. The region above the front exhibited a cutoff wavelength of  $\lambda = 492.5$  nm corresponding to nanocrystals of sizes of  $d \leq 6.4$  nm. Therefore, there are blue shifts of 47.5 and 19.5 nm in wavelength as compared to 512 nm corresponding to bulk CdS. The absorbance of CdS in the pulse was also measured at an interval of one week. The results are shown in Figure 7. It is clear that no significant change in the absorption spectrum of

the propagating pulse was noted. This signifies that the average size of the CdS nanoparticles in the propagating pulse, which although decelerating, is not changing as it propagates further. Similar findings were obtained for the larger particles left in the wake of the pulse, where no growth of particles was ever observed even after a lapse of months. This, as we later discuss, is mainly attributed to the role of the gelatin matrix in controlling the size, the overall particle size distribution of the particles, and the crystalline phase of the CdS particle.

**3.3.3. Steady-State and Lifetime Photoluminescence.** As was mentioned before, the CdS particles trailing with the propagating pulse exhibit weak fluorescence in the visible region. However, CdS particles inside the pulse were strongly fluorescing when excited by UV radiation, and their room-temperature photoluminescence spectra were also measured at different time intervals. This is shown in Figure 8, where the fluorescence spectra of the propagating pulse in tube 1 were taken on days 2, 4, 8, and 14. Contrary to the preparation of CdS nanocrystals in organic solvents,<sup>41</sup> whose photoluminescence spectra are dominated by strong blue band-edge emission bands with  $\lambda_{\text{em}}$  in the vicinity of 400 nm, the CdS nanocrystals in the pulse exhibit a broad emission band at  $\lambda_{\text{em}} = 560$  nm. This emission is attributed to recombination via surface-localized states or shallow traps<sup>42</sup> due to transitions from states of localized defects to the valence band. A slight red shift was seen in the emission maxima of the propagating pulse with time ( $\lambda_{\text{em}} = 560$  nm on day 2 and 566 nm on day 22). This indicates that the shallow traps persist as the pulse propagates, indicating the everlasting strong interaction between the nanocluster of CdS and the gelatin matrix. There are also weaker bands observed in Figure 8 in the region between 600 and 700 nm (indicated by the symbol +). These are also due to shallow traps due to a cadmium vacancies coupled to a chlorine that substitutes an adjacent sulfur.<sup>43</sup> These traps seem not to change with time. All of this seems to indicate an Ostwald ripening mechanism whereby the small crystals or nuclei forming in the pulse grow with time to form larger crystals behind. The fact that these larger crystals quench the photoluminescence of the gelatin matrix indicates that these crystals are structurally different from those in the pulse.

In order to understand the reasons behind the weak emission of the region above the pulse, we performed time-correlated single-photon counting (TCSPC) measurements on the two regions (pulse and front). Figure 9 shows the emission decay

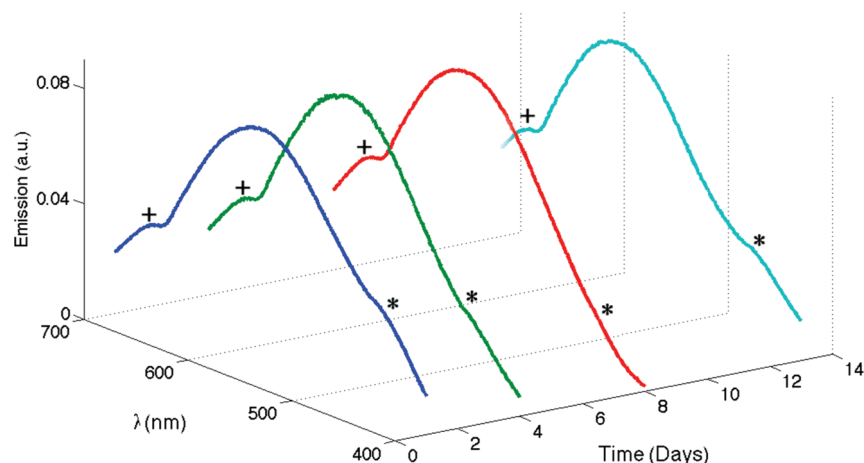


**Figure 8.** Emission spectra of the propagating pulse for tube 1 (50 mM Na<sub>2</sub>S, 2 mM CdCl<sub>2</sub>, and 2.5 mM mercaptoethanol) on days 2, 4, 8, and 14,  $\lambda_{\text{exc}} = 350$  nm. The shoulders indicated by \* at around 447 nm in all spectra are due to weak emission from the gelatin matrix. The shoulders indicated by + between 600 and 700 nm are due to emission from CdCl traps.

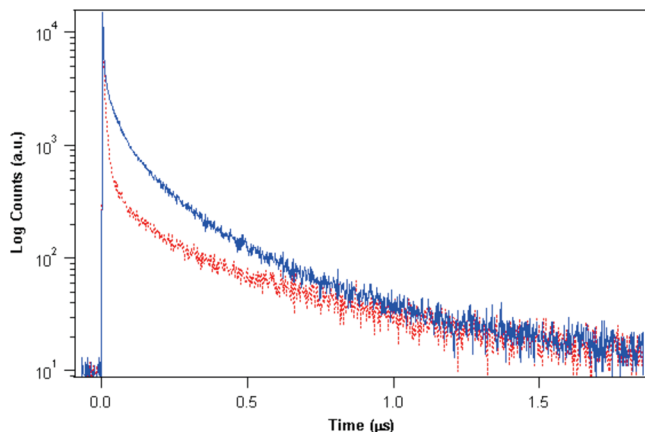


**Figure 9.** Lifetime emission spectra of the (solid blue) pulse and (dashed red) front,  $\lambda_{\text{ex}} = 405 \text{ nm}$  and  $\lambda_{\text{em}} = 560 \text{ nm}$ .

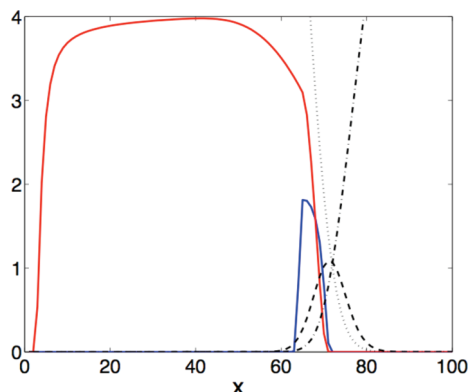


**Figure 10.** Snapshot at time  $= 4 \times 10^6$  of densities  $\tilde{\rho}$  (blue curve) and  $\rho$  (red curve), reaction rate  $R$  (dashed curve), outer concentration  $S$  (dotted curve), and inner concentration (dash-dotted curve) as a function of distance  $x$ . The initial conditions are  $Cd_0 = 10$  and  $S_0 = 400$ . Other parameters are  $k = 1 \times 10^{-5}$ ,  $D_S = D_{Cd} = 1 \times 10^{-5}$ ,  $D_c = 2 \times 10^{-4}$ ,  $c_1 = 3.0$ ,  $c_2 = c_3 = 2.1$ ,  $\alpha = \beta = \delta = 1 \times 10^{-2}$ , and  $\gamma = 1 \times 10^{-3}$ .

profiles for the pulse and the front. The emission decays of the two regions deviate from the single-exponential behavior as expected due to the existence of different sizes of the CdS nanoparticles within each region and due to emission evolving from different traps within a single CdS nanoparticle. However, what can be inferred from the TCSPC measurements is the fact that the emission of the “smaller” CdS nanoparticles in the front, if any exist, are quenched by either an electron-transfer or energy-transfer reaction to the “larger” nanoparticles. Such charge-transfer reactions can explain the weaker emission of the front when compared to that of the pulse.

#### 4. Model

Theoretical approaches to the modeling of the  $A + B \rightarrow C$  reaction–diffusion system span scaling ansatz and perturbation techniques,<sup>8,13,31,32</sup> mean-field theory,<sup>4,10</sup> as well as Monte Carlo<sup>9</sup> and other numerical methods.<sup>2,5,11,14</sup> In their seminal work, Gálfy and Rácz<sup>8</sup> carried out an analytical calculation of the precipitate front properties through the coupling of diffusion to second-order reaction kinetics ( $A + B \rightarrow C$ ). They found that the distance traveled by the front scales as  $t^{1/2}$ , while the pulse width scales as  $t^{1/6}$  and the rate of product formation as  $t^{-2/3}$ . Using scaling perturbation techniques, Taitelbaum et al.<sup>31,32</sup> found various time dependences of the reaction center as a function of the ratio of diffusion coefficients and the ratio of initial

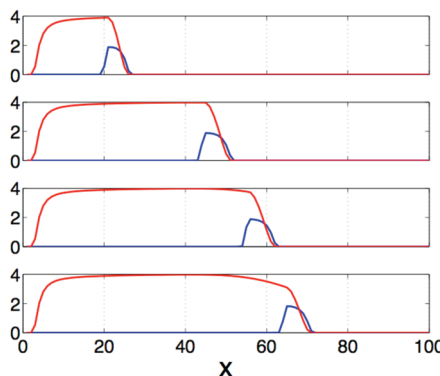


**Figure 11.** Time evolution of the densities densities  $\tilde{\rho}$  (blue curve) and  $\rho$  (red curve) at four different times, from top to bottom,  $t = 5 \times 10^5$ ,  $1 \times 10^6$ ,  $3 \times 10^6$ , and  $4 \times 10^6$ . Initial conditions and parameters are the same as those in Figure 10.

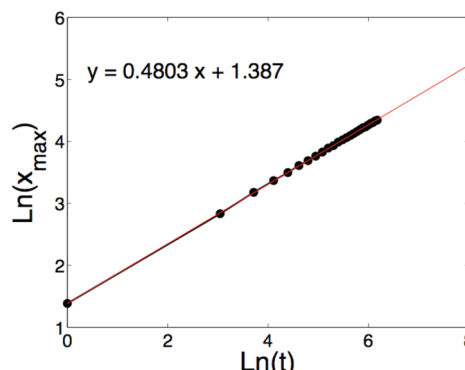


**Figure 12.** The ln–ln plot for the location of the front's tip,  $x_{\text{max}}$ , as a function of time  $t$ . The slope of the fit is 0.4803, close to  $1/2$ . Initial conditions and parameters are the same as those in Figure 10.

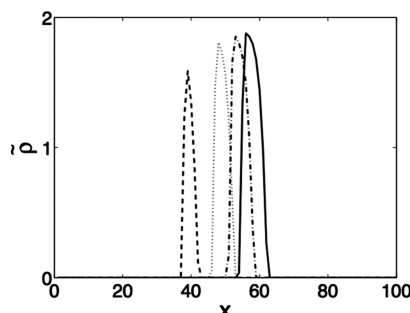


**Figure 13.** Effect of the outer concentration on the speed of the pulse; the higher the outer concentration, the faster the pulse. Snapshot of the density  $\tilde{\rho}$ , as a function of space at a given time  $t = 5 \times 10^6$  and  $Cd_0 = 10$ ;  $S_0 = 100$  (dashed),  $200$  (dotted),  $300$  (dash-dotted), and  $400$  (solid).

concentrations of the reacting species. They noted different crossovers with transient scaling exponents of  $1/2$  (short times) and  $3/2$  (intermediate times) before reaching the asymptotic regime of  $1/2$ . In some cases, extrema in the time evolution of the reaction center at intermediate times were theoretically predicted and confirmed experimentally.<sup>32</sup> On another note, the obtained crossover result is particularly interesting as it captures the features of front propagation in a number of studied chemical reaction systems.<sup>1,8,13,31,32</sup> In a reaction–diffusion system with reactants ( $\text{Ca}^{2+}$ –Ca green) initially separated by a semipermeable membrane, Park et al.<sup>7</sup> observed a dynamic transition of the front characteristics between several time regimes, an early time, an intermediate time, and an asymptotic time regime. The crossover times between these regimes were found to depend

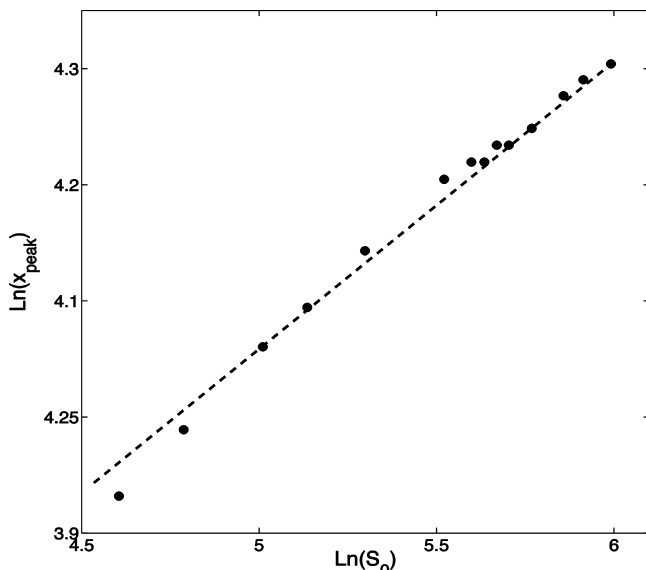


**Figure 14.** The  $\ln-\ln$  plot for the location of the peak of the density of nuclei  $x_{\text{peak}}$  as a function of the outer concentration  $S_0$ . The fitted line has a slope of 0.25.

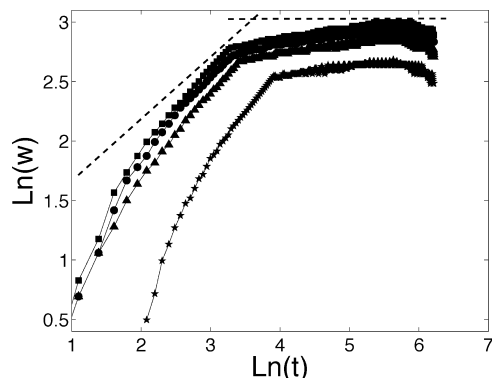
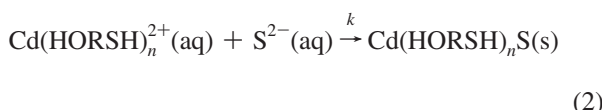
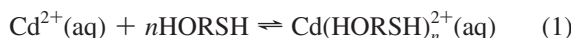


**Figure 15.** The  $\ln-\ln$  plot of the width of the pulse as a function of time at different initial conditions,  $S_0 = 100$  (star), 200 (triangle), 300 (dots), and 400 (squares). The dashed lines have slopes of  $1/2$  and  $0$ .

on the membrane thickness. In this section, we are interested in the dynamics of the pulse and the pulse-front interaction due to nucleation and growth of CdS clusters rather than the dynamics of the reaction zone by itself, which, in fact, is extensively studied as mentioned above. We would also like to report any existing power law which would characterize the dynamics of the pulse. Therefore, we are here pushing the complexity of the problem one step further.

Consider the following reaction of the precipitation of CdS in the gel medium



where HORSH represents the capping agent mercaptoethanol. It readily binds to  $\text{Cd}^{2+}$  to form a pre-equilibrium as shown in reaction 1. When the capped cadmium ions denoted as  $\text{Cd}(\text{HORSH})_n^{2+}(\text{aq})$  encounter the sulfide ions, they precipitate

as Cd (HORSH)<sub>n</sub>S(s) according to reaction 2, with a particulate size in the nano range. For simplicity, we denote the precipitate as CdS(s). The  $k$  denotes the rate constant of the precipitation reaction. Since diffusion is coupled to these chemical reactions, we shall construct reaction-diffusion equations that describe this system. For that purpose, we adopt the following simplified reaction scheme



and then adhere to the model of Müller and Polezhaev (MP)<sup>45</sup> in the description of the evolution of the precipitate. The species CdS(aq) appearing in reaction 3 represents the dissolved salt, which is an intermediate phase. It can nucleate and grow, leading to the solid precipitate CdS(s), which is usually described by a continuous spatiotemporal particle size distribution function. However, in the MP model, two particle sizes, small and large, are used to characterize the precipitate. Let  $\tilde{\rho}$  denote the average density of solid salt in the form of small particles or nuclei and  $\rho$  the average density of solid salt in the form of large particles;  $\tilde{\rho}$  and  $\rho$  are, in fact, quantities of matter in the nuclei and in particles contained in a unit volume, respectively. Let  $c$  be the concentration of the dissolved salt CdS(aq). If  $c$  exceeds some critical value  $c_3$ , small particles (nuclei) nucleate in the salt solution with a rate of nucleation of  $v_1$ . If  $c$  exceeds some other parameter  $c_2$ , nuclei are transformed into large particles at a rate of  $v_3$ ; otherwise, they dissolve at a rate of  $v_2$ . Finally, if  $c$  exceeds a certain value  $c_1$ , large particles grow at a rate of  $v_4$ . This model is simplified and only assumes that there are only two competing particle sizes, small nuclei and large particles, which is far from giving a complete picture of what is going on at the molecular level during the nucleation-growth-ripening of the CdS clusters. In addition, this model is not deficient if we want to study the evolution of the actual particle size distribution; however, it can easily be extended to include many average densities or even a continuous particle distribution function.

**4.1. Evolution Equations.** In order to simplify the mathematical notation, we introduce the following variables:  $Cd = [\text{Cd}^{2+}(\text{aq})]$ ,  $S = [\text{S}^{2-}(\text{aq})]$ , and  $P = \text{CdS}(\text{s})$ . The square bracket [i] denotes the molar concentration of species i. The conservation equations for the electrolyte concentrations diffusing and reacting according to reaction 3 are given by

$$\frac{\partial Cd}{\partial t} = D_{\text{Cd}} \nabla^2 Cd - k Cd \times S \quad (4)$$

$$\frac{\partial S}{\partial t} = D_S \nabla^2 S - k Cd \times S \quad (5)$$

where  $D_{\text{Cd}}$  and  $D_S$  are the diffusion coefficients of  $\text{Cd}^{2+}$  and  $\text{S}^{2-}$ , respectively;  $\nabla^2$  is the Laplacian; and  $k$  is the precipitation rate constant. The concentration of dissolved salt,  $c$ , is given by

$$\frac{\partial c}{\partial t} = D_c \nabla^2 c + k Cd \times S - v_1(c) + v_2(c)\tilde{\rho} - v_4(c)\rho \quad (6)$$

where  $D_c$  is the diffusion coefficient of dissolved salt  $c$ .

Using the definitions of the rates  $v_i$  ( $i = 1-4$ ) from the previous section, the dynamics of the average densities,  $\tilde{\rho}$  and  $\rho$ , are given by the following equations

$$\frac{\partial \tilde{\rho}}{\partial t} = v_1(c) - [v_2(c) + v_3(c)]\tilde{\rho} \quad (7)$$

$$\frac{\partial \rho}{\partial t} = v_3(c)\tilde{\rho} + v_4(c)\rho \quad (8)$$

We still have to specify the explicit form of the rate function  $v_i(c)$  to complete the description of the problem. It is shown<sup>45,46</sup> that the shape of the  $v_i(c)$ 's does not affect the qualitative behavior of the result. Therefore, we only assume that they are monotonous functions of  $c$  as follows

$$v_1(c) = \alpha(c - c_3)\theta(c - c_3) \quad (9)$$

$$v_2(c) = \beta(c_2 - c)\theta(c_2 - c) \quad (10)$$

$$v_3(c) = \gamma(c - c_2)\theta(c - c_2) \quad (11)$$

$$v_4(c) = \delta(c - c_1)\theta(c - c_1) \quad (12)$$

where  $\alpha, \beta, \gamma$ , and  $\delta$  are rate constants and  $\theta(x)$  is the Heaviside function. The nucleation rate  $v_1$  in eq 9 assumes a linear dependence on the concentration  $c$ , but we also tried a power law dependence on  $c$ , and we did not note any quantitative difference for all of the cases that are reported in this paper. The main reason behind this fact is that our model is a postnucleation model where nucleation does not play an important role like in prenucleation models, the front results from the interplay between diffusion, growth, and Ostwald ripening.

**4.2. Numerical Results.** Equations 4–8 were solved numerically with the following initial conditions

$$\begin{aligned} Cd(t=0, x) &= Cd_0\theta(x - L/2) \\ S(t=0, x) &= S_0\theta(L/2 - x), \\ \tilde{\rho}(t=0, x) &= \rho(t=0, x) = c(t=0, x) = 0 \end{aligned} \quad (13)$$

and the following no-flux boundary conditions

$$\mathbf{n} \cdot \nabla Cd \Big|_{x=L} = \mathbf{n} \cdot \nabla S \Big|_{x=L} = \mathbf{n} \cdot \nabla c \Big|_{x=L} = 0 \quad (14)$$

where  $x$  is the spatial independent variable and  $L$  is the length of the tube in which the reaction is taking place. The length  $L$  was partitioned into an equally spaced mesh of 400 grid points. Equations 4–8 were then discretized according to a second-order centered finite difference scheme to compute the Laplacians. The resulting ordinary differential equations were solved using Gear's method<sup>47</sup> for stiff-differential equations. We decreased the size of the mesh by increasing the number of grid points to 800, keeping the same length. The results did not change qualitatively.

In Figure 10, we show a snapshot of the evolution of the concentrations  $Cd$  and  $S$ , defined above, of the diffusing species

and the resulting particle densities of CdS nuclei  $\tilde{\rho}$  and the density of large particles  $\rho$ . The dashed line represents the reaction rate defined as  $R(x,t) = kCd \times S$  that is defined by Gálfi and Rácz.<sup>8</sup> It is noteworthy that the pulse ( $\tilde{\rho}$ ) as well as the tip of the front ( $\rho$ ) both lie within the reaction zone defined by  $R(x,t)$  at any given instant. The density  $\rho$  represents a front extending from near the boundary toward the end of the tube. The density of nuclei  $\tilde{\rho}$  looks like a pulse that leads the way. In Figure 11, the evolution of the densities is shown at four different times. It is important to note that for any outer or inner concentrations, part of the pulse lies always ahead of the front. This intersection defines a constant area at any time during the evolution. The density  $\tilde{\rho}$  also extends inside of the density  $\rho$ . This reproduces the experimental behavior where the nuclei are concentrated in a small region (pulse), although there are faintly fluorescing nuclei trailing behind, and lie inside of the front region.

The distance traveled by the front is measured as the coordinate of the most advanced nonzero value of the front,  $x_{\max}$ . It exhibits a diffusive  $t^{1/2}$  behavior as shown in the  $\ln-\ln$  plot in Figure 12, where the slope is found to be 0.48, very close to 1/2. For any initial outer concentration, this power law is recovered. The quantity  $x_{\text{peak}}$ , which corresponds to the location of the peak of the density nuclei  $\tilde{\rho}$  (particles in the pulse), should exhibit a power law similar to that shown in Figure 12 for the quantity  $x_{\max}$  location of the tip of the pulse), that is, a power law of exponent close to 1/2. The reason is due to the fact that the width of the pulse is constant, and the power law exhibited by  $x_{\text{peak}}$  should be very close to that of  $x_{\max}$ . To check this, we determined from the  $\ln-\ln$  plot of  $x_{\text{peak}}$  versus time (same parameters as those in Figure 10) the exponent, which was found to be 0.53, close to 1/2, with a correlation coefficient of 0.996. This early time dynamics was analytically confirmed by Taitelbaum et al.<sup>32</sup> Other results by Koza and Taitelbaum<sup>30</sup> revealed that the motion of  $x_f$  can exhibit extrema in time where the front switches direction and also a situation of a stationary front after a single change of direction.

Figure 13 exhibits the effect of the outer concentration on the speed of the pulse. The higher the outer concentration, the farther the distance traveled, that is, the higher the speed. On the other hand, when the inner concentration is increased for a given outer concentration, the speed of the pulse decreases. In general, when the difference between the initial concentrations increases, the speed of the propagating pulse increases too. Since our model lacks detailed information about the interaction between CdS and the capping agent, we were not able to find the oscillations in the speed obtained in the experiment above. However, it seems that the capping agent is interacting with the  $\text{Cd}^{2+}$  ions, causing the concentration of the free uncapped ions to vary accordingly (least interaction is at 40 mM mercaptoethanol for the two different inner concentrations), and consequently, the difference between the concentrations of inner free  $\text{Cd}^{2+}$  ions and outer  $\text{S}^{2-}$  ions varies, causing the observed fluctuation in the speed of the pulse as a function of the capping agent. We also found a power law behavior for the location of the maximum  $x_{\text{peak}}$  of the density  $\tilde{\rho}$  (i.e., pulse) as a function of the outer initial concentration  $S_0$

$$x_{\text{peak}} \sim S_0^c \quad (15)$$

which exhibits  $c = 0.25$  or 1/4. A slight deviation from the straight line is observed at initial concentrations,  $S_0$ , close to 100. These results are shown in Figure 14. The width of the

pulse was also shown to obey a power law as a function of time

$$w \sim t^a$$

with crossover between early times where  $a = 0.35$  (very close to  $1/3$ ) and intermediate times where  $a = 0$ , that is, fixed width, as shown in the  $\ln - \ln$  plot in Figure 15. It is noteworthy to see that the width is almost independent of the outer concentrations, ranging from  $200-400$ ; however, a noticeable decrease is exhibited for lower outer concentrations around  $100$ . We found that the inner concentration affects the crossover point. The lower the inner concentration, the further the crossover point. It is also worth mentioning that the short-time reaction width exponent was found to be  $1/2$  in the mean-field theoretical results of the simple system  $A + B \rightarrow C$ , as compared to the  $1/3$  obtained in our simulation, with a crossover to  $1/6$  in the long-time regime.<sup>31</sup>

## 5. Conclusion

The motivation of this work extends from (1) reporting of a new pulse-exhibiting reaction–diffusion system; (2) the early stage dynamics of Liesegang banding; and (3) the synthesis and size control of CdS quantum dots. First, we presented in this paper a new system exhibiting pulse propagation and pulse–front interaction. The system consists of sulfide ions diffusing into a gel containing cadmium ions capped with mercaptoethanol. We showed that we can use the scaling laws of the speed and the width of the pulse to shed light on the chemical mechanism that is taking place.

The product consisted of nanoparticles of CdS. Such a system, because of its spectroscopic and optoelectronic properties, enabled us to understand the early stages of nucleation leading to growth and ripening in this reaction–diffusion system. The mechanism of formation of such nanoparticles is shown to take place in the gel through a pulse propagation consisting of fluorescing nuclei of sizes of at least  $4$  nm leaving behind a front consisting of larger crystals of sizes greater than  $6$  nm using a spatial Ostwald ripening mechanism. Therefore, this system could be appealing because it would allow us to study the early time dynamics in Liesegang banding systems. We have not reported in this work that under certain conditions, the pulse leaves in its wake Liesegang bands instead of the reported homogeneous front. We can thereby monitor the nucleation, growth, and ripening of those bands as was deemed possible from this work. Last, this work provided a new method to synthesize CdS quantum dots. We are now investigating how to control the size and size distribution of the CdS nanoparticles by varying the initial supersaturation, the nature and concentration of the gel, and the concentration of the capping agent.

We also presented a model based on nucleation, growth, and size competition. This model was shown to successfully reproduce many of the observed experimental results related to the speed of the pulse as well as its width and interaction with the front. Many power laws were also derived especially at early and intermediate times. This encouraged us to verify these laws in more thorough experiments with focus on the early time regime. We will use this system to study the mechanism of formation of Liesegang banding, prenucleation theories based on the Ostwald–Prager (OP)<sup>44,48</sup> supersaturation–nucleation–depletion cycle and postnucleation theories developed by Ross,<sup>49,50</sup> Ortoleva,<sup>51,52</sup> and their co-workers based on the competitive growth of the particles (CPG theory). We are also

interested in studying the effect of an electric field on the pulse and front propagation<sup>53,54</sup> as well as the particle growth and crystal phase change.

**Acknowledgment.** This work was supported by grants from the University Research Board (URB), American University of Beirut, and the Lebanese Council for Scientific Research (LCNRS).

## References and Notes

- (1) Yen, A.; Lee Koo, Y.-E.; Kopelman, R. Experimental Study of a Crossover from Nonclassical to Classical Chemical Kinetics: An Elementary and Reversible  $A + B \rightleftharpoons C$  Reaction–Diffusion Process in a Capillary. *Phys. Rev. E* **1996**, *54*, 2447.
- (2) Taitelbaum, H.; Vilensky, B.; Lin, A.; Yen, A.; Lee Koo, Y.-E.; Kopelman, R. Competing Reactions with Initially Separated Components. *Phys. Rev. Lett.* **1996**, *77*, 1640.
- (3) López Cabarcos, E.; Chein-Shiu Kuo, Scala, A.; Bansil, R. Crossover between Spatially Confined Precipitation and Periodic Pattern Formation in Reaction–Diffusion Systems. *Phys. Rev. Lett.* **1996**, *77*, 2834.
- (4) Park, S. H.; Parus, S.; Kopelman, R.; Taitelbaum, H. Gel-Free Experiments of Reaction–Diffusion Front Kinetics. *Phys. Rev. E* **2001**, *64*, 055102R.
- (5) Baroud, Ch. N.; Okkels, F.; Ménétrier, L.; Tabeling, P. Reaction–Diffusion Dynamics: Confrontation Between Theory and Experiment in a Microfluidic Reactor. *Phys. Rev. E* **2003**, *67*, 060104R.
- (6) Lee Koo, Y.-E.; Kopelman, R. Space- and Time-Resolved Diffusion-Limited Binary Reaction Kinetics in Capillaries: Experimental Observation of Segregation, Anomalous Exponents, and Depletion Zone. *J. Stat. Phys.* **1991**, *65*, 893.
- (7) Park, S. H.; Peng, H.; Kopelman, R.; Taitelbaum, H. Dynamical Localization-Delocalization Transition of the Reaction–Diffusion Front at a Semipermeable Cellulose Membrane. *Phys. Rev. E* **2007**, *75*, 026107.
- (8) Gálfi, L.; Rácz, Z. Properties of the Reaction Front in an  $A + B \rightarrow C$  Type Reaction–Diffusion Process. *Phys. Rev. A* **1988**, *38*, 3151–3154.
- (9) Larralde, H.; Araujo, M.; Havlin, Sh.; Stanley, H. E. Reaction Front for  $A + B \rightarrow C$  Diffusion–Reaction Systems with Initially Separated Reactants. *Phys. Rev. A* **1992**, *46*, 855.
- (10) Barkema, G. T.; Howard, M. J.; Cardy, J. L. Reaction–Diffusion Front for  $A + B \rightarrow \phi$  in One Dimension. *Phys. Rev. E* **1996**, *53*, R2017.
- (11) Sancho, J. M.; Romero, A. H.; Lindenberg, K.; Sagués, F.; Reigada, R.; Lacasta, A. M. A + B → 0 Reaction with Different Initial Patterns. *J. Phys. Chem.* **1996**, *100*, 19066.
- (12) Chopard, B.; Droz, M.; Karapiperis, T.; Rácz, A. Properties of the reaction front in a reversible  $A + B \rightleftharpoons C$  reaction–diffusion process. *Phys. Rev. E* **1993**, *47*, R43.
- (13) Sinder, M.; Pelleg, J. Asymptotic Properties of a Reversible  $A + B \rightleftharpoons C$  (Static) Reaction–Diffusion Process with Initially Separated Reactants. *Phys. Rev. E* **2000**, *62*, 3340.
- (14) Pribyl, M.; Snita, D.; Marek, M. Nonlinear phenomena and qualitative evolution of risk of clogging in a capillary microreactor under imposed electric field. *Chem. Eng. J.* **2005**, *105*, 99.
- (15) Field, R.; Burger, M., Eds. *Oscillations and Traveling Waves in Chemical Systems*; Wiley: New York, 1985.
- (16) *Phys. Chem. Chem. Phys.*, A special Issue on Nonlinear Kinetics **2002**, *4*, 1253–1386.
- (17) Avnir, D.; Kagan, M. Spatial Structures Generated by Chemical Reactions at Interfaces. *Nature* **1984**, *307*, 717.
- (18) (a) Kravchenko, V. V.; Medvinskii, A. B.; Reshetilov, A. N.; Ivanitskii, G. R. *Dokl. Akad. Nauk* **1999**, *364*, 114–116. (b) Kravchenko, V. V.; Medvinskii, A. B.; Reshetilov, A. N.; Ivanitskii, G. R. *Dokl. Akad. Nauk* **1999**, *364*, 687–689.
- (19) Ortoleva, P. *Geochemical Self-Organization*; Oxford University Press: New York, 1994.
- (20) Jamtveit, B.; Meakin, P., Eds. *Growth, Dissolution and Pattern Formation in Geosystems*; Kluwer Academic Publishers: Dordrecht, The Netherlands, 1999.
- (21) Msharrafieh, M.; Al-Ghoul, M.; Sultan, R. *Simulation of Geochemical Banding in Acidification-Precipitation Experiments In-Situ, in Complexus Mundi: Emergent Patterns in Nature*; Novak, M. M., Ed.; World Scientific: Singapore, 2006; pp 225–236.
- (22) Bao, Y.; Nicholson, P. S. Constant Current Electrophoretic Infiltration Deposition of Fiber-Reinforced Ceramic Composites. *J. Am. Ceram. Soc.* **2007**, *90*, 1063–1070.
- (23) Backfolk, K.; Lagerge, S.; Rosenholm, J. The Influence of Stabilizing Agents on the Interaction between Styrene/Butadiene Latex and Calcium Carbonate: A Calorimetric and a Dynamic Electrokinetic Study. *J. Colloid Interface Sci.* **2002**, *254*, 8.

- (24) Chong, T.; Sheikholeslami, R. Thermodynamics and Kinetics for mixed calcium carbonate and calcium sulfate precipitation. *Chem. Eng. Sci.* **2001**, *56*, 5391.
- (25) Magnico, P. Impact of Dynamic Processes on the Coupling between Fluid Transport and Precipitate Deposition. *Chem. Eng. Sci.* **2000**, *55*, 4323.
- (26) Hampton, J.; Savage, S. Computer Modeling of Filter Pressing and Clogging in Random Tube Network. *Chem. Eng. Sci.* **1993**, *48*, 1601.
- (27) Liesegang, R. E. Chemische Fernwirkung. *Lieseg. Photograph. Arch.* **1896**, *37*, 305. continued in *37*, 331.
- (28) Dee, G. T. Patterns Produced by Precipitation at a Moving Reaction Front. *Phys. Rev. Lett.* **1986**, *57*, 275.
- (29) Henisch, H. K. *Crystals in Gels and Liesegang Rings*; Cambridge University Press: Cambridge, U.K., 1988.
- (30) Koza, K.; Taitelbaum, H. Motion of the reaction front in A + B → C reaction–diffusion system. *Phys. Rev. E* **1996**, *54*, R1040.
- (31) Taitelbaum, H.; Havlin, Sh.; Kiefer, J. E.; Trus, B.; Weiss, G. H. Some Properties of the A + B → C Reaction–Diffusion System with Initially Separated Components. *J. Stat. Phys.* **1991**, *65*, 873.
- (32) Taitelbaum, H.; Lee Koo, Y.-E.; Havlin, Sh.; Kopelman, R.; Weiss, G. H. Exotic Behavior of the Reaction Front in the A + B → C Reaction–Diffusion System. *Phys. Rev. A* **1992**, *46*, 2151.
- (33) Lamberti, C., Ed. *Characterization of Semiconductor Heterostructures and Nanostructures*; Elsevier: Amsterdam, The Netherlands, 2008.
- (34) Kundu, M.; Khosravi, A. A.; Kulkarni, A. A. Synthesis and study of organically capped ultra small clusters of cadmium sulphide. *J. Mater. Sci.* **1997**, *32*, 245–258.
- (35) Murakoshi, K.; Hosokawa, H.; Saitoh, M.; Wada, Y.; Sakata, T.; Mori, H.; Mitsunobu, S.; Yanagida, S. Preparation of size-controlled hexagonal CdS nanocrystallites and the characteristics of their surface structures. *J. Chem. Soc., Faraday Trans.* **1998**, *94*, 579–586.
- (36) Kalandaragh, Y. A.; Muradov, M. B.; Mamedov, R. K.; Khodayari, A. Growth process and investigation of some physical properties of CdS nanocrystals formed in polymer matrix by successive ionic layer adsorption and reaction (SILAR) method. *J. Cryst. Growth* **2007**, *305*, 175–180.
- (37) Hecht, I.; Moran, Y.; Taitelbaum, H. Reaction–diffusion front width anomalies in disordered media. *Phys. Rev. E* **2006**, *73*, 051109–1–6.
- (38) Bazant, M.; Stone, H. A. Asymptotics of reaction–diffusion fronts with one static and one diffusing reactant. *Physica D* **2000**, *147*, 95–121.
- (39) Z. Jiang, Z.; Ebner, C. Simulation study of reaction fronts. *Phys. Rev. A* **1990**, *42*(, 7483–7486.
- (40) Banerjee, R.; Jayakrishnan, R.; Ayyub, P. Effect of the size-induced structural transformation on the band gap in CdS nanoparticles. *J. Phys.: Condens. Matter* **2000**, *12*, 10647.
- (41) Zezza, F.; Comparelli, R.; Striccoli, M.; Curri, M. L.; Tommasi, R.; Agostiano, A.; Della Monica, M. High quality CdS nanocrystals: surface effects. *Synth. Met.* **2003**, *139*, 597–600.
- (42) Okamoto, S.; Kanemitsu, Y.; Hosokawa, H.; Murakoshi, C. K.; Yanagida, S. Photoluminescence from surface-capped CdS Nanocrystals by selective excitation. *Solid State Commun.* **1998**, *105*, 7–11.
- (43) Bing, L.; Xu, G. Q.; Gan, L. M.; Chew, C. H.; Li, W. S.; Shen, Z. X. Photoluminescence and structural characteristics of CdS nanoclusters synthesised by hydrothermal microemulsion. *J. Appl. Phys.* **2001**, *89*, 1059–1063.
- (44) Ostwald, Wi. A-Linien von R. E. Liesegang, review. *Lehrbuch der Allgemeinen Chemie*, 2. Aufl., Band II, 2. Teil: Verwandtschaftslehre; Engelmann: Leipzig, Germany, 1899; p 779.
- (45) Müller, S. C.; Polezhaev, A. A. Complexity of precipitation patterns: comparison of simulation with experiment. *Chaos* **1994**, *4*, 631.
- (46) L’Heureux, I. Elimination of the intermediate colloidal product in models of periodic precipitation patterns. *Phys. Lett. A* **1999**, *263*, 70.
- (47) Kahaner, D.; Moler, C.; Nash, S. *Numerical Methods and Software*; Prentice Hall: Englewood Cliffs, NJ, 1989.
- (48) Prager, S. Periodic Precipitation. *J. Chem. Phys.* **1956**, *25*, 279.
- (49) Kai, S.; Müller, S. C.; Ross, J. Measurements of Temporal and Spatial Sequences of Events in Periodic Precipitation Processes. *J. Chem. Phys.* **1982**, *76*, 1392.
- (50) Lovett, R.; Ortoleva, P.; Ross, J. Kinetic Instabilities in First-Order Phase Transitions. *J. Chem. Phys.* **1978**, *69*, 947.
- (51) Feinn, D.; Scalf, W.; Ortoleva, P.; Schmidt, S.; Wolff, M. Spontaneous Pattern Formation in Precipitating Systems. *J. Chem. Phys.* **1978**, *69*, 27.
- (52) Feeney, R.; Ortoleva, P.; Strickholm, P.; Schmidt, S.; Chadam, J. Periodic Precipitation and Coarsening Waves: Applications of the Competitive Particle Growth Model. *J. Chem. Phys.* **1983**, *78*, 1293.
- (53) Bena, I.; Coppex, F.; Droz, M.; Rácz, Z. Front Motion in an A + B → C Type Reaction–Diffusion Process: Effects of an Electric Field. *J. Chem. Phys.* **2005**, *122*, 024512.
- (54) Yu, J.; Neretnieks, I. Modeling of Transport and Reaction Processes in a Porous Medium in an Electric Field. *Chem. Eng. Sci.* **1996**, *51*, 4355.

JP9022647